



Low-dose aberration corrected cryo-electron microscopy of organic specimens

James E. Evans^{a,d,*}, Crispin Hetherington^b, Angus Kirkland^b, Lan-Yun Chang^b, Henning Stahlberg^a, Nigel Browning^{c,d}

^a Molecular and Cellular Biology, University of California at Davis, 1 Shields Ave., Davis, CA 95616, USA

^b Department of Materials, Oxford University, Parks Road, Oxford OX1 3PH, UK

^c Department of Chemical Engineering and Materials Science, University of California, 1 Shields Avenue, Davis, CA 95616, USA

^d Materials Science and Technology Division, Chemistry, Materials and Life Sciences Directorate, Lawrence Livermore National Laboratory, Livermore, CA 94550, USA

ARTICLE INFO

Article history:

Received 19 July 2007
Received in revised form
28 May 2008
Accepted 17 June 2008

Keywords:

Aberration correction
Electron microscopy
TEM
Cryo-EM

ABSTRACT

Spherical aberration (C_s) correction in the transmission electron microscope has enabled sub-angstrom resolution imaging of inorganic materials. To achieve similar resolution for radiation-sensitive organic materials requires the microscope to be operated under hybrid conditions: low electron dose illumination of the specimen at liquid nitrogen temperature and low defocus values. Initial images from standard inorganic and organic test specimens have indicated that under these conditions C_s -correction can provide a significant improvement in resolution (to less than 0.16 nm) for direct imaging of organic samples.

© 2008 Published by Elsevier B.V.

1. Introduction

Determining organic structures (such as biological proteins) by transmission electron microscopy (TEM) is primarily resolution limited by the very low signal-to-noise ratio in recorded images. This arises from the high radiation sensitivity and low atomic number of organic materials. While methods exist to image chemically fixed and/or stained biological samples, these techniques generally do not achieve sub-nanometer resolution. In order to record images at near-atomic resolution, biological materials need to remain hydrated to preserve structural integrity. Specimen preparation methods such as sugar embedding and cryo-electron microscopy (cryo-EM) [1] help to maintain the atomic scale structural integrity of biological samples under high-resolution imaging conditions. However, these sample preparation methods further reduce the signal-to-noise ratio due to similar densities between the sample and the surrounding solution. Therefore, to obtain sufficient contrast, vitrified biological samples are usually observed under phase contrast bright field imaging conditions with a highly under-focused objective lens (typically 10–35 times the Scherzer defocus) [2]. This defocus condition leads to a large number of reversals in the contrast

transfer function (CTF) of the TEM [3] at high spatial frequency, which leads to gaps in the information transfer.

For conventional bright-field TEM, cryo-EM images of biological samples are normally recorded under a compromise condition that favors either the generation of sufficient contrast or the preservation of high-resolution information. For both two-dimensional (2D) crystals and single particles, signal averaging is often performed on large numbers of identical samples, which were originally imaged under conditions yielding lower contrast but higher resolution. Although such computational averaging of the images helps alleviate signal-to-noise issues, it requires homogeneous samples. However, most biological samples are somewhat heterogeneous in many aspects including purity, relative stability, and oligomerization state. Even 2D crystals exhibit twinning, dislocations and other defects, which will disrupt the observed homogeneity. While many of these issues arise from the specimen itself and sample preparation techniques, advances are continuously being made in these areas and promise to provide higher quality samples to be imaged in the future. For current instrumentation, all of these factors combine to limit the attainable spatial resolution to around 0.19–0.6 nm for membrane proteins reconstituted in a lipid bilayer and arranged as 2D crystals [4–6], and 0.4–1.2 nm for soluble proteins treated as single particles [7,8]. Both of these resolution limits for biological materials are significantly lower than the resolutions routinely obtained for radiation resistant inorganic samples, where a spatial

* Corresponding author. Tel.: +1 530 754 8285; fax: +1 530 752 3085.
E-mail address: JEEvans@ucdavis.edu (J.E. Evans).

resolution of 80 pm has been demonstrated by using spherical aberration (C_s) correction with future developments expected to extend this to 50 pm [9–15].

Application of aberration corrected imaging to achieve sub-angstrom resolution with organic or biological samples is only theoretically limited by the image contrast of the sample under low-dose conditions and its sensitivity to the electron beam under high-resolution imaging conditions. However, most microscopes currently used for biological imaging (operating at 200 kV) possess a C_s in the range of 2–4 mm, which intrinsically limits the directly interpretable resolution to around 0.2 nm with an information limit of ca. 0.14 nm. While contrast is generally a paramount issue when imaging samples in cryo-EM, the need to observe low spatial frequencies for highly periodic samples, such as aligned 2D crystals, is removed, and the ultimate resolution of a C_s -corrected microscope for organic samples can be tested.

The major motivation for these experiments was to merge standard materials sciences and biological imaging methods. While using the minimal dose system (MDS) is standard protocol for structural biologists, it is rarely used for the imaging of inorganic specimens, where it can be very useful for imaging low atomic number or radiation-sensitive materials samples such as zeolites, ceramics, and polymer-embedded quantum dots. Similarly, aberration correction is becoming a standard technology for materials scientists, yet is relatively unexplored in the imaging of biological samples where it could be used to enhance the spatial coherence envelope to increase overall resolution. Due to this divide in methodology, it was necessary to test the capability of the microscope for utilizing MDS and aberration correction at the same time.

In this paper, we present the first results that test the achievable spatial resolution for organic samples using a C_s -corrected TEM. These tests were performed on a JEOL JEM-2200FS, equipped with dual C_s -correctors for both the condenser and objective lens systems, together with an in-column Omega energy filter [11]. For the purposes of this paper, only the contribution of the objective lens C_s -corrector towards imaging of organic samples is reported.

2. Experimental setup

2.1. Samples

2.1.1. Silicon

A Si sample (a standard sample for high-resolution tests [11]), was prepared by crushing a fragment of a Si wafer under methanol. The resultant suspension was allowed to settle and a drop was allowed to dry onto a TEM grid coated with a holey amorphous carbon support film.

2.1.2. Paraffin

Paraffin crystals were prepared at room temperature as previously described [16]. Briefly, a 3 μ l drop of a 1/3 saturated solution of paraffin in hexane (courtesy of R. Glaeser and D. Typke) was added to a continuous carbon coated 400-mesh copper grid (Ted Pella, Inc., CA, USA).

2.2. TEM imaging

The JEM-2200FS column incorporates a Schottky field-emission-gun, an omega-type electron energy filter and C_s -correctors for both the image and probe forming lenses [11]. The microscope was operated at an accelerating voltage of 200 kV and the anti-

contamination device was cooled with liquid nitrogen prior to sample insertion. Both samples were transferred to the microscope using a Gatan 636 cooling holder. This holder does not have transfer shutter blades that cover the grid during transfer into the column. Following insertion of the holder at room temperature, the samples were cooled to LN₂ temperature in the column and allowed to thermally equilibrate for 60 min. After thermal equilibration of the sample, a standard alignment of the microscope was performed. The objective lens C_s -corrector (CETCOR) was aligned using a Zemlin Tableaux to measure the coefficients of the wave aberration function to third order [11]. For the data reported here, the spherical aberration was set to a value of -5μ m and the defocus was initially adjusted to the Gaussian condition; all other coefficients were adjusted to zero values within the limits set by the measurement accuracy. Images were recorded utilizing a low-dose protocol on a Gatan 894 Ultrascan (2048 pixel \times 2048 pixel) CCD camera, operated with the Digital Micrograph 3.0 software. Beam-tilt in combination with the deflection coils of the energy filter were used to achieve the deflected “Focus” alignment for low-dose imaging. Images were recorded under low-dose conditions with a nominal magnification of 300,000 \times and defocus values of -5 and -36 nm for silicon and paraffin, respectively. Electron dose calibration was performed using a Faraday cage at 300,000 \times magnification.

2.3. Verification of the paraffin sample quality

To ensure that the test organic sample possessed sufficient high-resolution information, we recorded diffraction patterns of several paraffin crystals (Fig. 1), using a simplified low-dose data collection scheme. Paraffin crystals were identified using the shadow image produced by defocused diffraction mode. Diffraction patterns were then collected in selected area diffraction mode, with only coarse focusing of the diffraction pattern. This low-dose procedure was used to ensure that all high-resolution components, if present, were recorded. As the recorded diffraction patterns were not precisely focused, each reflection split. Fig. 1a shows the observed three-fold splitting of each reflection in the diffraction pattern which was attributed to the crystal being twinned and not precisely focused. Fig. 1b depicts a map of observed (closed circle) reflections with the $\{-4,4\}$ reflection corresponding to a spacing of 0.103 nm. These results established that the paraffin crystals were well ordered and that sample preparation would not be a limiting factor for this study.

2.4. Image processing

TEM images of organic cryo-EM samples typically have a very low signal-to-noise ratio. Hence, computer image processing is often applied to extract structural information from such images using data from a multitude of equivalent samples. In particular, images of crystalline samples enable efficient computer processing by Fourier data extraction: From a calculated Fourier transform, amplitudes and phases for each identified reciprocal lattice location are measured, corrected for the effect of the instrumental CTF, and used for the generation of a final reconstruction [17].

This commonly applied method requires a sample with a perfectly straight lattice. Since biological samples are rarely ordered with the necessary quality, and since most TEM images show slight distortions, including pincushion and spiral distortions, numerical image processing is used to initially unbend such distortions in the recorded image, before Fourier data extraction is applied [18,19]. In this process, a lattice unbending profile is determined and iteratively refined, which is then used to correct

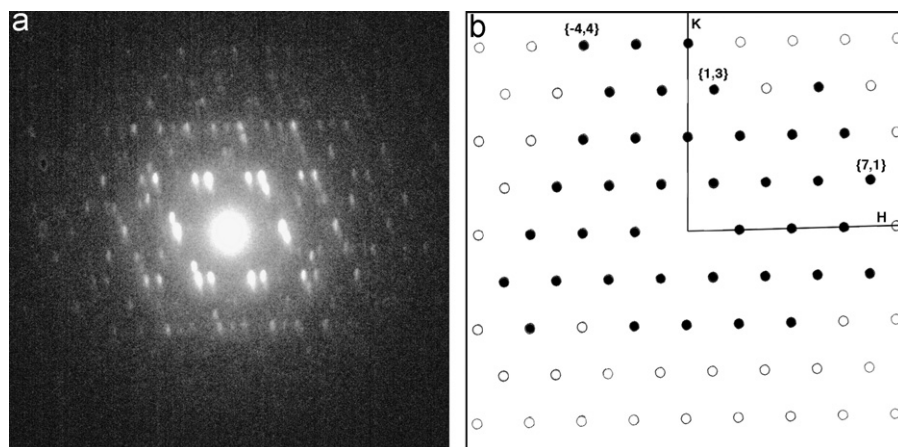


Fig. 1. Electron diffraction of a paraffin sample: (a) Defocused diffraction pattern of a paraffin crystal showing the reflection splitting described in the text. (b) Map of reflections visible in (a). Open circles indicate the overall lattice while closed circles show the positions of observed reflections.

strain and defects in the image. The final unbent image is then Fourier transformed, after which the Fourier transform shows significantly sharpened lattice reflections. This process also allows recovery of reciprocal lattice information from reflections that are too blurred in the Fourier transform of the raw image for reliable evaluation.

2.4.1. Image processing of $\langle 110 \rangle$ Si

Lattice distortions for the image of $\langle 110 \rangle$ Si were determined by lattice-node tracking within a cross-correlation map between the raw image and a reference pattern, which was iteratively established by a Fourier filtering process. The distortion plot showed a single coherent crystalline pattern with homogeneous distortions that were re-interpolated to a coherent unbending plot as shown in Fig. 2a.

Values for amplitudes and phases for each reciprocal lattice reflection in the Fourier transform of the unbent image were evaluated, together with an average background amplitude value around each reflection. Fig. 2b shows the Fourier transform of the unbent image, with the signal-to-noise ratio of each reflection indicated by the IQ value [20].

2.4.2. Image processing of paraffin

Lattice distortions for the images of paraffin were similarly determined as described above. The original unprocessed images of paraffin described in Figs. 5a and 6a contained approximately 1200 and 2800 unit cells, respectively. The distortion plots for these images showed single coherent crystalline patterns (Figs. 2c and e) and revealed local deformations of the ideal lattice, as typical for organic samples. The lattice distortions were used to unbend the original image data thereby producing a final projection map of the unit cell. Figs. 2d and f show the Fourier transforms of the unbent image, with the signal-to-noise ratio of each spot indicated by the IQ value [20].

2.5. Image simulations

TEM images of both $\langle 110 \rangle$ Si and paraffin were simulated using the calibrated experimental conditions to compare with experimental data. The image intensity simulation was divided into two parts: the specimen exit wave function calculations [21] and the image formation using SEMPER [22]. The former was calculated using the multi-slice formalism [23] which is a dynamical fast electron scattering algorithm for arbitrary objects. Subsequently, high-resolution TEM images were simulated using a

general formula describing the image intensity I [24] as

$$I(k) = \int_{k'} \psi(k+k')\psi(k') \exp(-2\pi i(\chi(k+k') - \chi(k'))) E_s(k+k', k') E_d(k+k', k') dk'$$

where ψ is the Fourier transform of the specimen exit wave function, χ the objective lens aberration function, and E_s and E_d the spatial and temporal coherence envelope functions, respectively. As images taken under low-dose conditions have low signal-to-noise ratios, Poisson noise was subsequently added to the images to model the effects of the detector and shot noise arising from the low number of electrons contributing to the image. The level of this additional noise was calculated by taking the average electron dose used to record the experimental images into account. The MTF of the CCD camera was not included in the simulation since it does not give rise to the limiting envelope function when matching the experimental conditions and corresponding pixel size.

3. Results and discussion

As already noted, standard operating conditions for direct imaging of biological samples using cryo-EM target a balance between generating sufficient contrast at low spatial frequencies for adequate visualization (Fig. 3a) while maintaining high spatial resolution (Fig. 3b). The effective result of this compromise is a significant resolution limitation as defined within the CTF by the information transfer limit and point resolution. While the CTF benefits from the low Cs and defocus characteristic of aberration corrected imaging, (Fig. 3d) it does not provide the high contrast of low-resolution components that are generally required for imaging biological samples. Recently proposed mechanisms for improving the visibility of biological samples, at or near the Gaussian focus, incorporate a phase shift device located in the back focal plane of the objective lens [25–27]. These devices are designed to introduce an additional phase shift in the central beam relative to the scattered electrons, or *vice versa*, in order to increase the transfer of low spatial frequencies. While these devices can potentially increase the low-resolution image contrast, the high-resolution information transfer is not significantly improved (Fig. 3e). Therefore, only the combination of a phase shift device (to enhance low spatial frequencies) together with aberration correction (for transfer of high spatial frequencies without any contrast reversals [9,13,28,29]) will provide adequate information transfer for atomic resolution imaging of biological

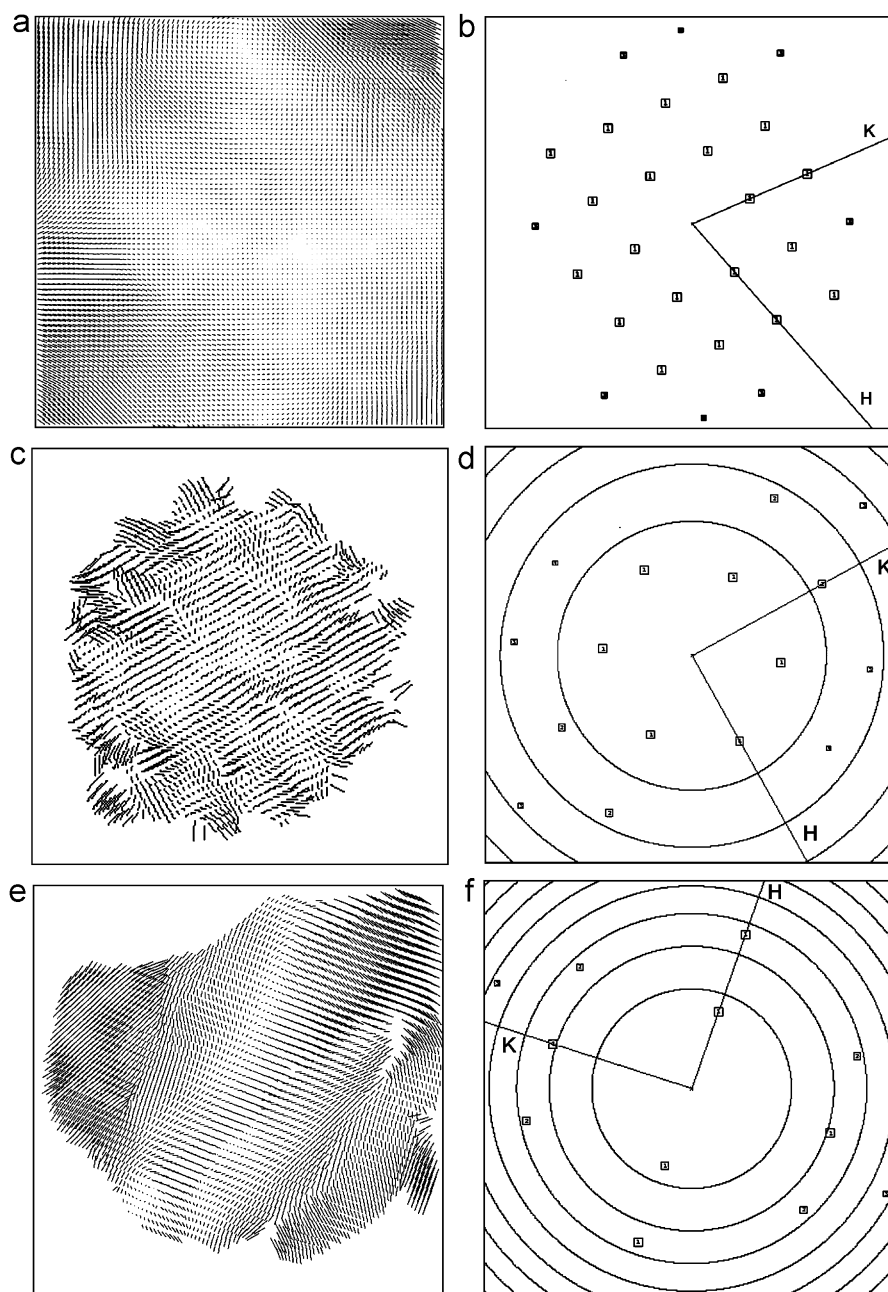


Fig. 2. Image unbending plots: (a) Re-interpolated lattice unbending plot used to correct lattice image distortions for the image of $\langle 110 \rangle$ Si shown in Fig. 4a. (b) The IQ plot for the Fourier transformation of Fig. 4a after unbending. The signal-to-noise ratio of each spot is indicated by an IQ value that ranges from 1 (large squares) to 4 (smallest squares). Reflection $\{1,1,5\}$ has an IQ value of 4 at a resolution of 0.11 nm. (c) Lattice unbending plot used to correct lattice image distortions for the image of paraffin shown in Fig. 5a. (d) The IQ plot for the Fourier transformation of Fig. 5a after image unbending reveals an IQ value of 3 for the $\{-1,3\}$ reflection of paraffin. (e) Lattice unbending plot used to correct lattice image distortions for the image of paraffin shown in Fig. 6a. (f) The IQ plot for the Fourier transformation of Fig. 6a after image unbending reveals an IQ value of 3 for the $\{1,3\}$ reflection of paraffin. (a, c, e) Each line segment is 10 times exaggerated and depicts how individual image segments were translocated during image unbending.

samples (Fig. 3f), while maintaining the required transfer of low spatial frequencies. Phase shifting devices capable of delivering the required performance are currently being developed. However, the performance of aberration corrected instruments under low electron dose conditions, as required for biological and organic samples, has not previously been determined.

To test the effectiveness of aberration correction under low electron dose conditions we recorded images of $\langle 110 \rangle$ oriented Si and paraffin. The former is a representative standard inorganic material often used for high-resolution tests and calibration [11]. For our purposes as reported here, this was used to test the

performance of the microscope under low-dose and low-temperature conditions on a sample independent of beam sensitivity. In addition, as a representative biological sample, we also recorded images of *n*-paraffin, tetratetracontane ($C_{44}H_{90}$), which is a low-atomic-number organic sample that has similar beam sensitivity and contrast to many protein samples. Paraffin has been used as a resolution standard for biological techniques since it is capable of self-assembling into mono-lamellar crystals of Pca2₁ symmetry with orthorhombic unit cell dimensions of $a = 0.75$ nm $b = 0.495$ nm, and $\alpha = 90^\circ$ [16–30]. Moreover, previous reports have demonstrated direct imaging of paraffin at

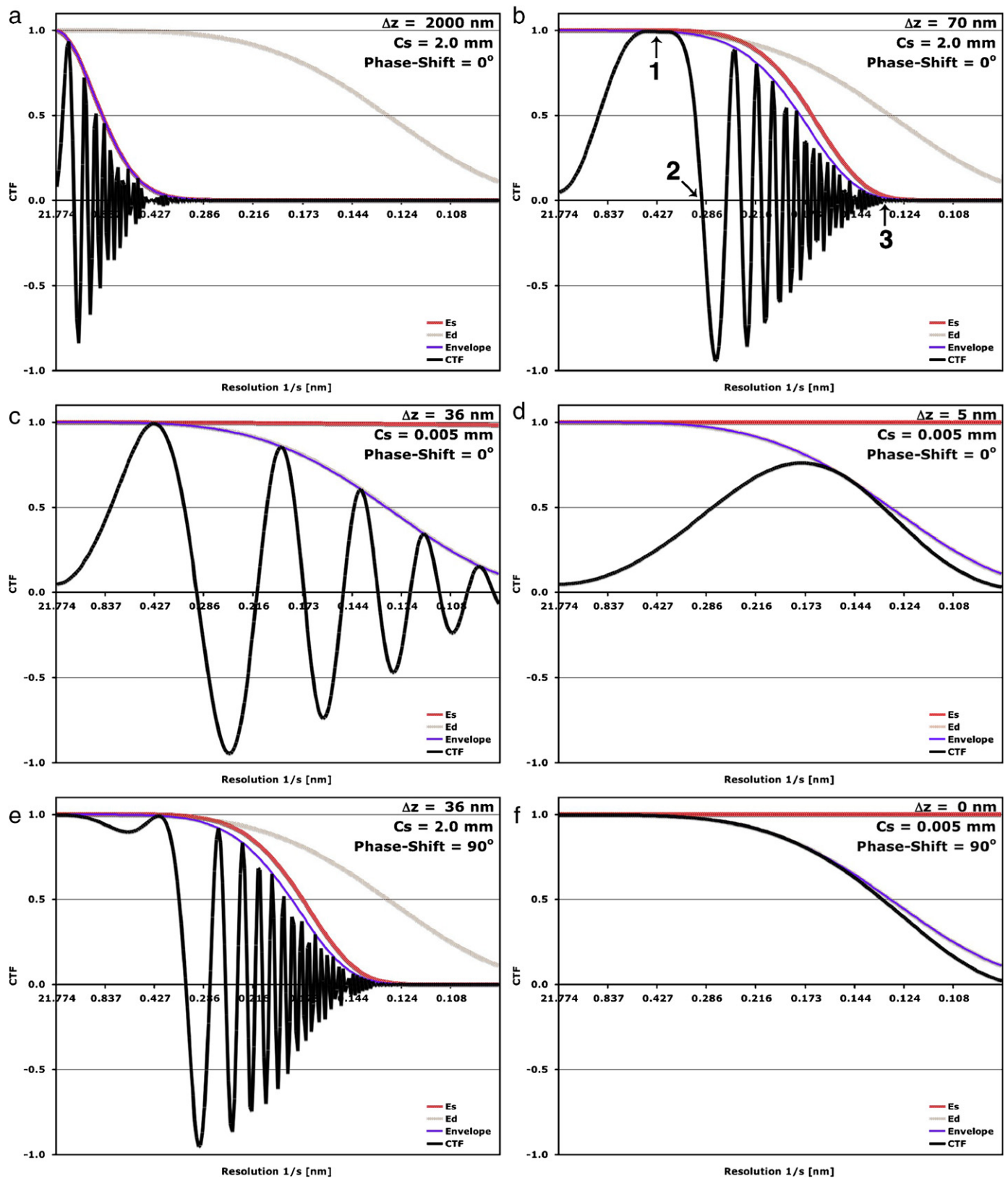


Fig. 3. Contrast transfer functions (CTF) for a JEOL JEM 2200FS under different imaging conditions plotted to a maximum resolution of 0.1 nm. The influence of atomic scattering profiles is ignored in these plots. Envelope functions for partial spatial (E_s) and temporal (E_d) coherence are shown together with the resulting total envelope function. Parameters used are acceleration voltage = 200 kV, $\alpha_i = 0.1$ mrad, $\Delta E = 0.8$ eV, and $C_c = 1.46$ mm. (a, b) Typical CTFs for high-contrast imaging for biological (a) and (b) inorganic samples without aberration correction or phase-shift devices. Arrows indicate the spatial frequency transferred with highest contrast (1), the point resolution (2), and the information limit (3) of the microscope under these conditions. (c) CTF of the aberration corrected instrument used in this study for imaging Paraffin (36 nm underfocus). (d) CTF of the aberration corrected instrument used in this study for imaging Silicon (5 nm underfocus). (e) Typical CTF of an instrument equipped with a phase shift device, but without correction for spherical aberration. (f) Achievable CTF of an instrument with a phase shift device and C_s -correction for the objective lens.

0.2 nm resolution using a helium cooled microscope operating at 100 kV [30] and a liquid-nitrogen cooled microscope operating under spot-scanning conditions at 400 kV [16].

Experimental low-dose imaging [31] requires rapid changes between three operational modes (“search”, “focus”, and “exposure”). These modes are such that “search” allows the identification of sample positions of interest (at low magnification and therefore low illumination intensity). The “focus” mode then allows the user to locate the correct objective lens defocus at a sample location adjacent to the specific area of interest. Finally, the “exposure” mode is used for the acquisition of the final image during which the electron dose is limited to $\sim 5\text{--}10\text{ e}^-/\text{\AA}^2$ when working at LN₂ temperature and can be up to $20\text{ e}^-/\text{\AA}^2$ when a 2D crystal of membrane proteins is imaged at liquid helium temperatures [32]. The JEM-2200FS microscope used in this study has suitable MDS software that records three independent memory settings for lens currents, beam-shift and image-shift values, allowing convenient switching between these imaging modes.

To test the imaging performance of the JEM-2200FS under low-dose cryo-EM conditions, images of a $\langle 110 \rangle$ Si crystal were recorded under conditions equivalent to those used for imaging biological samples. The use of silicon in place of a biological sample served as a positive control to verify the performance of the imaging aberration corrector and in particular the reliability of

its alignment under low-dose conditions. Using minimal dose techniques, we were able to record a direct image of the cooled sample (Fig. 4a) that shows a lattice reflection in the power spectrum (Fig. 4b) corresponding to the $\{1,1,5\}$ reflection, at a spacing of 0.11 nm. However, the intensity of the $\{4,0,0\}$ reflection is weak and hence the characteristic “dumbbell” separation in Si $\langle 110 \rangle$ is not clearly visible in the unprocessed images. To ensure that the raw image and processed projection map (representing the underlying signal in the absence of noise) were not artifacts, we also simulated an image of $\langle 110 \rangle$ Si by calculating the exit plane wavefunction and forming the image using experimental parameters. The simulation (Fig. 4d) shows excellent agreement with both the raw micrograph and the processed unit cell projection (Fig. 4c). Although these results were facilitated by the high contrast and radiation resistance of the silicon sample, they confirm the information transfer capability and overall performance of the instrument at LN₂ temperature under a low-dose protocol.

During imaging of the low-atomic-number, low-contrast sample paraffin, the growth of a continuously thickening ice contamination layer on top of the specimen reduced the overall signal-to-noise ratio of the beam-sensitive paraffin during high-resolution data acquisition. This contamination growth occurred during the temperature equilibration phase of the specimen and was attributed to residual water and/or carbon in the vacuum

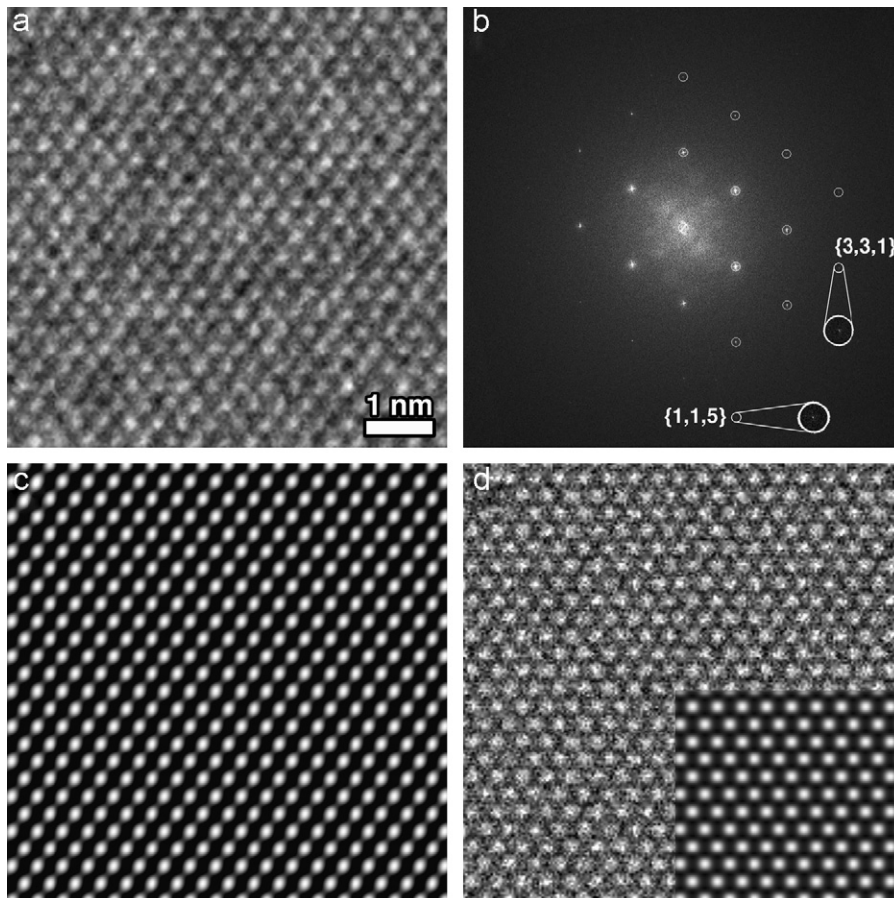


Fig. 4. Spherical aberration corrected images of a $\langle 110 \rangle$ Si sample: (a) Direct image of $\langle 110 \rangle$ Si acquired on the JEM-2200FS with the TEM aberration corrector operating under low dose and cryo conditions. Imaging parameters were accelerating voltage = 200 kV, $C_s = 0.005$ mm, defocus = -5 nm (underfocus), nominal direct magnification = $300,000\times$. (b) Fourier transform of the raw image in (a). The $\{3,3,1\}$ and $\{1,1,5\}$ reflections correspond to spacings at 0.136 and 0.11 nm, respectively. (c) Reconstruction of the projection map after image processing [18,19]. The raw image was computationally corrected for small lattice distortions; the resulting “unbent” image was Fourier transformed, and values for amplitudes and phases of the now sharpened diffraction peaks were extracted. These were corrected for the CTF of the instrument and used to synthesize the reconstructed image reproduced in (c). Si atom pairs appear black in all images. (d) Simulated image of Si $\langle 110 \rangle$. The simulation was calculated using parameters corresponding to the experimental conditions described above with the additional Poisson noise to model low-dose conditions. Inset is a simulated image in the absence of noise.

system of the JEM 2200FS. It should be noted that ice contamination was also present during the imaging of the silicon sample. However, in contrast to a biological sample, we were able to evaporate the ice with the electron beam without damaging the high-resolution or high-contrast components of the silicon sample prior to imaging.

Despite these limitations, we were successful in acquiring direct images of paraffin under low-dose operating conditions. The images show clear resolution of the paraffin lattice (Fig. 5a) with reflections in the calculated power spectrum at a spacing of 0.25 nm resolution (Fig. 5b). Image processing as described earlier, produced a reconstruction of the projection map at 0.16 nm resolution (Fig. 5c). It should be noted that the $\{-1,3\}$ reflection with a 0.16 nm spacing has an IQ value of 3, which corresponds to a signal-to-noise ratio of 2.33 using the average of the surrounding non-reflection pixels as the basis for the background noise level. Furthermore, comparison of the original image (Fig. 5a) with a simulation of the paraffin lattice (Fig. 5d) shows good agreement providing further support for our analysis. However, the agreement between the image and simulation applies to the unit cell parameters and molecular positions, but does not show the relative rotation of each molecule representative of a herringbone arrangement. We believe this is due to a lack of sufficient resolution along both axes to observe the rotation.

When imaging the paraffin sample, we intentionally utilized a higher defocus than that used for imaging silicon. The variance in defocus was due to the fact that Si has better inherent contrast

that allows it to be imaged closer to Gaussian defocus than paraffin. The images of Si were recorded to optimize the microscope performance and to demonstrate high-resolution information transfer limit under aberration corrected, low-dose conditions. For paraffin (composed of low-atomic-number elements) a slightly higher defocus was chosen to increase low-resolution contrast by having the CTF maximum occur near the resolution of the first-order reflection at 1/0.412 nm. The favoring of low-frequency information, although arguably not necessary for imaging paraffin, is required for imaging more standard biological samples and was tested in this experiment. In the future, the incorporation of a phase-shift device will address the issue of reduced contrast of low spatial frequencies and should allow imaging of paraffin and other organic samples at close to Gaussian defocus.

A second image of paraffin (Fig. 6) depicts lattice reflections at 0.20 nm in the raw FFT prior to any unbending. This image shows a crystal with slightly different lattice dimensions compared with other paraffin crystals. The unit cell is elongated along the b -axis with a dimension of 0.88 nm rather than 0.75 nm [16–30] and lacks the normal $\{1,1\}$ and $\{-1,1\}$ reflections. Nevertheless, both the $\{0,2\}$ and $\{2,2\}$ reflections reported in earlier papers are visible in the power spectrum of the raw image and match the highest known published resolution recorded for paraffin using direct imaging. After unbending, the $\{1,3\}$ reflection at a resolution of 0.16 nm has an IQ value of 3. It should be noted that we recorded several images of this type of crystal polymorph and the fringes

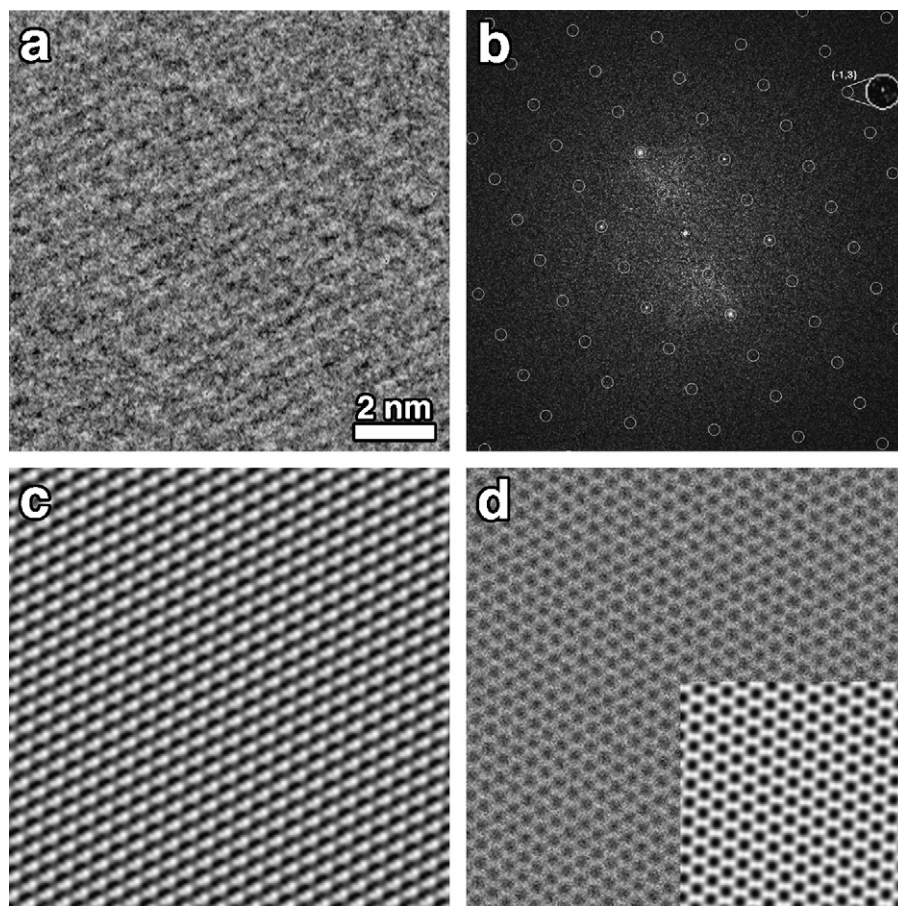


Fig. 5. Images of a two-dimensional paraffin crystal recorded under low-dose cryo conditions. Imaging parameters were accelerating voltage = 200 kV, $C_s = 0.005$ mm, defocus = -36 nm (underfocus), nominal direct magnification = $300,000\times$: (a) Original image. (b) Calculated power spectrum of (a) before (left) and after (right) crystallographic lattice unbending, as described for Fig. 4. Circles indicate the crystal lattice. The $\{-1,3\}$ reflection corresponds to a spacing of 0.16 nm. (c) Reconstruction of the projection map after image processing [18,19]. (d) Simulated image of paraffin under C_s -corrected conditions based upon previously published results [34]. Inset is a simulated image in the absence of noise. Simulations performed as described in Fig. 4(d). Paraffin appears black in all images.

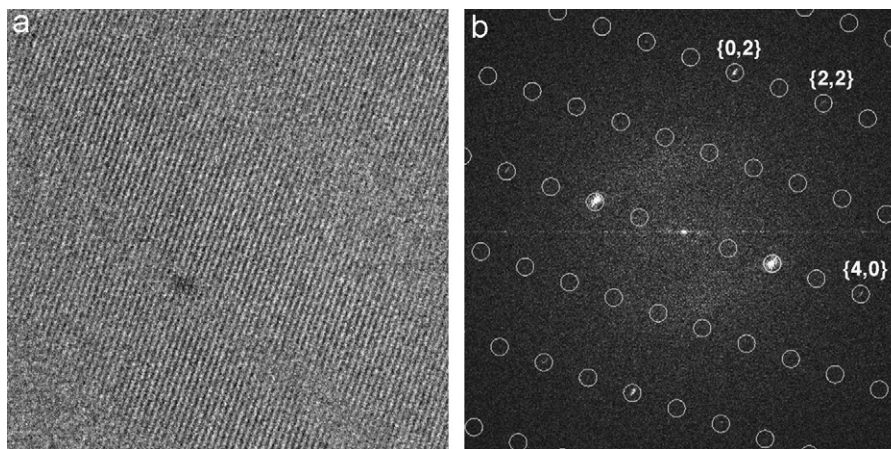


Fig. 6. Images of paraffin recorded under low-dose cryo conditions. Imaging parameters were as described for Fig. 5: (a) Original image. (b) Calculated power spectrum of the raw image. Circles indicate the crystal lattice. The $\{2,2\}$ reflection corresponds to a spacing of 0.2 nm.

visible in the direct image closely resemble those of paraffin in previously published reports [33]. In addition, the absence of reflections and elongation of the b -axis occurred similarly in these images, suggesting that this is likely formed by paraffin rather than a mineral contaminant.

As described above, our imaging efforts for paraffin produced several images that show the paraffin lattice in the direct image. Nevertheless, the success rate for recording such images was low, yet comparable to high-resolution cryo-EM imaging with an uncorrected instrument [16–30]. Taken together, these results show that a low-atomic-number radiation-sensitive organic sample can be imaged at near-atomic resolution using an aberration corrected microscope operated under low-dose operating conditions.

4. Conclusions

This paper documents the first direct experimental imaging of an organic sample with a spherical aberration corrected microscope operating under low-dose, cryogenic conditions. These results were based on images of organic and inorganic crystals to facilitate the interpretation and analysis of the effect of the aberration corrector. The imaging of a radiation resistant silicon specimen shows that the instrument can be operated under cryogenic conditions to at least 0.11 nm resolution using minimal electron dose techniques. It should be noted that an aberration corrected TEM is not suitable for “flood-beam” illumination imaging of highly tilted samples: The increasing defocus across the tilted sample would result in a CTF with strong oscillations and a limited envelope function in zones of stronger defocus, and these effects are worse when using an aberration corrected instrument, than when using an instrument without aberration correction. However, imaging of tilted specimens using spot-scanning illumination with per-spot-adjusted defocus would still benefit from aberration correction. In addition, the use of exit-wave reconstruction using a low-dose through-focal series may be another option to mitigate this problem albeit one requiring more stringent control of electron dose throughout the multiple image data set required. These are both techniques that seem possible continuations of the research described here but are beyond the scope of this report.

While it is clear that the use of an aberration corrected microscope extends the overall attainable resolution, it is not yet known what effect such a machine will have on other standard biological imaging techniques such as single particle reconstruc-

tion and tomography. These methods utilize imaging protocols that usually require large defocus values with the sample cross-section being imaged generally ranging from 50 to 250 nm in thickness. However, the preliminary results presented here suggest that even under these conditions and when combined with a phase-shift device, the overall resolution should be improved by removing the effect of the spherical aberration on image formation. Further experiments will be required to evaluate the usefulness of this technique for these methods. In addition, future incorporation of a chromatic aberration corrector should further extend the attainable resolution.

Despite possible unresolved issues of immediate applicability to thicker biological samples than 2D crystals, by converging microscope parameters appropriate to the imaging of both organic and inorganic materials, there now exist the methods and technology to visualize inorganic–organic interfaces and radiation-sensitive materials in the TEM with near-atomic resolution. The results presented here demonstrate the feasibility of aberration corrected imaging of biological samples under cryo-EM minimum dose conditions, and initiate the path towards the construction of an electron microscope platform that combines aberration correction with phase-shift devices, C_c correction and energy filters and monochromators. Such an instrument, under ideal conditions, could allow the same flexibility and sensitivity for imaging and analysis of organic samples that is currently available for inorganic materials.

Acknowledgments

The authors are grateful to R. Glaeser, D. Typke for providing the paraffin solution and for relevant discussions. This work was supported by the National Institute of Health (training Grant P32-GM07377) and by the US Department of Energy (Grant no. DE-FG02-03ER46057). AIK acknowledges financial support from the Engineering and Physical Sciences Research Council and from the Leverhulme Trust.

References

- [1] M. Adrian, J. Dubochet, J. Lepault, A.W. McDowell, *Nature* 308 (1984) 32.
- [2] O. Scherzer, *Appl. Phys.* 20 (1948) 20.
- [3] F. Thon, Phase contrast electron microscopy, in: U. Valdre (Ed.), *Electron Microscopy in Materials Science*, Academic Press, London, 1971 pp. 570–625.
- [4] T. Gonen, et al., *Nature* 438 (2005) 633.
- [5] R. Henderson, et al., *J. Mol. Biol.* 213 (1990) 899.
- [6] K. Murata, et al., *Nature* 407 (2000) 599.

- [7] W. Jiang, S.J. Ludtke, *Curr. Opin. Struct. Biol.* 15 (2005) 571.
- [8] S.J. Ludtke, D.H. Chen, J.L. Song, D.T. Chuang, W. Chiu, *Structure* 12 (2004) 1129.
- [9] P.E. Batson, N. Dellby, O.L. Krivanek, *Nature* 418 (2002) 617.
- [10] M. Haider, et al., *Ultramicroscopy* 75 (1998) 53.
- [11] J.L. Hutchison, et al., *Ultramicroscopy* 103 (2005) 7.
- [12] C.L. Jia, A. Thust, K. Urban, *Phys. Rev. Lett* 95 (2005) 225506.
- [13] M. Lentzen, et al., *Ultramicroscopy* 92 (2002) 233.
- [14] P.D. Nellist, et al., *Science* 305 (2004) 1741.
- [15] P.C. Tiemeijer, *Ultramicroscopy* 78 (1999) 53.
- [16] J. Brink, W. Chiu, *J. Microsc.* 161 (1991) 279.
- [17] R. Henderson, P.N. Unwin, *Nature* 257 (1975) 28.
- [18] R.A. Crowther, R. Henderson, J.M. Smith, *J. Struct. Biol.* 116 (1996) 9.
- [19] B. Gipson, X. Zeng, Z.Y. Zhang, H. Stahlberg, *J. Struct. Biol.* 157 (2007) 64.
- [20] R. Henderson, J.M. Baldwin, K.H. Downing, J. Lepault, F. Zemlin, *Ultramicroscopy* 19 (1986) 147.
- [21] E.J. Kirkland, *Advanced Computing in Electron Microscopy*, Plenum Press, New York, 1998.
- [22] W.O. Saxton, *J. Struct. Biol.* 116 (1996) 230.
- [23] J.M. Cowley, A.F. Moodie, *Acta Crystallogr.* 10 (1957) 609.
- [24] P.W. Hawkes, E. Kasper, *Principles of Electron Optics: Wave Optics*, Academic Press, London, 1994.
- [25] R. Cambie, K.H. Downing, D. Typke, R.M. Glaeser, J. Jin, *Ultramicroscopy* 107 (2007) 329.
- [26] R. Danev, K. Nagayama, *Ultramicroscopy* 88 (2001) 243.
- [27] E. Majorovits, et al., *Ultramicroscopy* 107 (2007) 213.
- [28] L.Y. Chang, A.I. Kirkland, J.M. Titchmarsh, *Ultramicroscopy* 106 (2006) 301.
- [29] R.H. Wade, *Ultramicroscopy* 46 (1992) 145.
- [30] F. Zemlin, E. Reuber, E. Beckmann, E. Zeitler, D.L. Dorset, *Science* 229 (1985) 461.
- [31] J. Hosoi, T. Matsuo, Y. Ishida, Y. Harada, *J. Electron. Microsc. (Tokyo)* 30 (1981) 1.
- [32] Y. Fujiyoshi, *Adv. Biophys.* 35 (1998) 25.
- [33] D.L. Dorset, *Proc. Natl. Acad. Sci. USA* 87 (1990) 8541.
- [34] I.-E. Mavrantza, D. Prentzas, V.G. Majorovits, C. Galiotis, *J. Chem. Phys.* 115 (2001) 3937.